JOURNAL OF GEOPHYSICAL RESEARCH, VOL. 112, D02206, doi:10.1029/2006JD007249, 2007

Analysis of reflectance spectra of UV-absorbing aerosol scenes measured by SCIAMACHY

M. de Graaf,[1] P. Stammes,[1] and E. A. A. Aben[2]

Received 2 March 2006; revised 7 September 2006; accepted 27 September 2006; published 25 January 2007.

[1] Reflectance spectra from 280–1750 nm of typical desert dust aerosol (DDA) and biomass burning aerosol (BBA) scenes over oceans are presented, measured by the space-borne spectrometer Scanning Imaging Absorption Spectrometer for Atmospheric Chartography (SCIAMACHY). DDA and BBA are both UV-absorbing aerosols, but their effect on the top-of-atmosphere (TOA) reflectance is different due to differences in the way mineral aerosols and smoke reflect and absorb radiation. Mineral aerosols are typically large, inert particles, found in warm, dry continental air. Smoke particles, on the other hand, are usually small particles, although often clustered, chemically very active and highly variable in composition. Moreover, BBA are hygroscopic and over oceans BBA were invariably found in cloudy scenes. TOA reflectance spectra of typical DDA and BBA scenes were analyzed, using radiative transfer simulations, and compared. The DDA spectrum was successfully simulated using a layer with a bimodal size distribution of mineral aerosols in a clear sky. The spectrum of the BBA scene, however, was determined by the interaction between cloud droplets and smoke particles, as is shown by simulations with a model of separate aerosol and cloud layers and models with internally and externally mixed aerosol/cloud layers. The occurrence of clouds in smoke scenes when sufficient water vapor is present usually prevents the detection of optical properties of these aerosol plumes using space-borne sensors. However, the Absorbing Aerosol Index (AAI), a UV color index, is not sensitive to scattering aerosols and clouds and can be used to detect these otherwise obscured aerosol plumes over clouds. The amount of absorption of radiation can be expressed using the absorption optical thickness. The absorption optical thickness in the DDA case was 0.42 (340 nm) and 0.14 (550 nm) for an aerosol layer of optical thickness 1.74 (550 nm). In the BBA case the absorption optical thickness was 0.18 (340 nm) and 0.10 (550 nm) for an aerosol/cloud layer of optical thickness 20.0 (550 nm). However, this reduced the cloud albedo by about 0.2 (340 nm) and 0.15 (550 nm). This method can be an important tool to estimate the global impact of absorption of shortwave radiation by smoke and industrial aerosols inside clouds.

Citation: de Graaf, M., P. Stammes, and E. A. A. Aben (2007), Analysis of reflectance spectra of UV-absorbing aerosol scenes measured by SCIAMACHY, *J. Geophys. Res.*, *112*, D02206, doi:10.1029/2006JD007249.

1. Introduction

[2] Our understanding of the effect of absorbing aerosols on the Earth's radiative budget has increased rapidly over recent years, especially since aerosols were identified as the largest uncertainty in modeling of climate radiative forcing [*Intergovernmental Panel on Climate Change*, 2001]. Absorbing aerosols reduce the irradiance at the surface and heat the atmosphere, thereby changing the lapse rate and vertical stability of the atmosphere, the hydrological cycle and circulation patterns. As cloud condensation nuclei (CCN), aerosols influence cloud growth rates, cloud lifetimes and precipitation intensities, and cloud albedo [e.g., *Twomey*, 1959b; *Albrecht*, 1989; *Hansen et al.*, 1997; *Haywood and Boucher*, 2000; *Ackerman et al.*, 2000; *Ramanathan et al.*, 2001; *Koren et al.*, 2004; *Lohmann and Feichter*, 2005].

[3] Aerosol properties can be characterized using ground-based measurements, for example using Sun-photometers and UV shadowband radiometers [e.g., *Krotkov et al.*, 2005]. However, owing to the short lifetime of atmospheric aerosols and heterogeneous horizontal distribution in the atmosphere, the continuous observations by satellite instruments are essential to monitor the global aerosol distributions and to assess their global radiation impact [*Kaufman et al.*, 2002].

[4] Satellite measurements, especially from the Total Ozone Mapping Experiment (TOMS), have been used extensively to study the global distribution of UV-absorbing

[1] Royal Netherlands Meteorological Institute (KNMI), De Bilt, Netherlands.
[2] Netherlands Institute for Space Research (SRON), Utrecht, Netherlands.

0148-0227/07/2006JD007249$09.00

aerosols [*Herman et al.*, 1997; *Torres et al.*, 1998]. The most important UV-absorbing aerosols are desert dust [e.g., *Chiapello et al.*, 1999; *Prospero et al.*, 2002; *Eckardt and Kuring*, 2005; *Darmenova et al.*, 2005; *Kaufman et al.*, 2005], biomass burning aerosols [e.g., *Gleason et al.*, 1998; *Hsu et al.*, 1999a; *Spichtinger et al.*, 2001; *Duncan et al.*, 2003; *Tanré et al.*, 2001], and volcanic aerosols [e.g., *Seftor et al.* 1997].

[5] Most current satellite aerosol retrieval algorithms rely on cloud screening before retrieving aerosol information [e.g., *Tanré et al.*, 1996; *Torres et al.*, 1998; *Veefkind et al.*, 2000; *Diner et al.*, 2001; *King*, 2003; *Hauser et al.*, 2005; *Kusmierczyk-Michulec and de Leeuw*, 2005]. This means a huge reduction of the global monitoring capability of satellite instruments, especially for those with large footprints. Furthermore, it prohibits remote sensing studies of cloud-aerosol interactions in those cases where clouds are present. However, the AAI, the scene color in the UV compared to that of a pure Rayleigh atmosphere, is insensitive to scattering aerosols and clouds [*Herman et al.*, 1997; *Torres et al.*, 1998; *De Graaf et al.*, 2005] and can be used to monitor the distribution of UV-absorbing aerosols in cloud-free and cloud-contaminated satellite data, both over land and ocean. It will detect aerosols over clouds but not under them unless the clouds are very thin.

[6] Using Global Ozone Monitoring Experiment (GOME) data, UV-absorbing aerosols have been shown to have a different effect on the TOA reflectance spectrum in the range of 300–800 nm for different aerosol types [*De Graaf et al.*, 2006]. Over land the reflectances at visible and longer wavelengths were mainly determined by the surface albedo, but over ocean all DDA scenes showed a relatively low reflectivity decreasing with wavelength, even when the mineralogical properties of desert dust can be very variable [*Sokolik and Toon*, 1999]. Ocean BBA scenes were much more variable. About half of the BBA scenes were also low reflectance scenes decreasing with wavelength, like the DDA scenes, while the other half showed a high reflectance increasing with wavelength. In this paper the reflectance spectra of a typical ocean DDA scene and a high reflectance ocean BBA scene are shown in a broad spectral range (280–1750 nm) with a high spectral resolution, using SCIAMACHY measurements. They are compared to reflectance spectra of clear sky scenes, and the effects of the aerosols on the TOA reflectance is modeled using radiative transfer simulations. The two cases of high aerosol loading scenes are a Saharan dust blowing event and a smoke scene from intense savanna fires over southwestern Africa. Both cases had a high AAI of around 3.5.

[7] Globally, the Sahara desert is the most important source of mineral aerosols. Several hundred million tons are estimated to be transported from the Sahara to the tropical North Atlantic Ocean and the Mediterranean Sea yearly [*D'Almeida*, 1986; *Prospero et al.*, 1996]. The most intense period of dust transport from the Saharan source region is in the boreal summer, but dust storms can be observed year-round [*De Graaf et al.*, 2006]. Saharan dust usually resides in a near-neutrally stable layer of dry air confined between two temperature inversion layers [*Prospero and Carlson*, 1972]. Because of this, the altitude-dependent AAI correlates well with Sun-photometer Aerosol Optical Thickness (AOT) measurements [*Hsu et al.*, 1999b]. Mineral aerosols provide surfaces for chemical reactions, change the concentration of other aerosols in the atmosphere, and affect cloud nucleation and optical properties. The iron content in desert dust plays a major role in ocean fertilization and oceanic carbon dioxide uptake, thereby affecting the global carbon budget [*Gao et al.*, 2001]. Dust transported to downwind terrestrial ecosystems can play a major role in soil formation and nutrient cycling [*Okin*, 2005].

[8] Spectrally, desert dust is a UV-absorbing aerosol, mainly due to the presence of hematite and other iron oxides. The imaginary part of the refractive index of desert dust is largest in the UV and decreases rapidly with wavelength, although the amount of absorption of desert dust in the UV is still under discussion [*Patterson et al.*, 1977; *Sinyuk et al.*, 2003; *Torres et al.*, 2005]. Since mineral particles are irregularly shaped, the optical modeling of desert dust is also a matter of debate. Mie theory, which is valid for homogeneous, spherical particles, is often used because it is well developed and good results can be produced [e.g., *Sinyuk et al.*, 2003; *Waquet et al.*, 2005]. As an alternative spheroids might be used, which reduces the amount of small mode particles in ground-based aerosol retrievals [*Dubovik et al.*, 2002a]. More complex particle-shape models are available [*Veihelmann et al.*, 2004], but these are computationally demanding and beyond the scope of this paper.

[9] Smoke is produced by annually recurring savanna fires in southwest Africa, during the local monsoonal dry period [*Herman et al.*, 1997; *Torres et al.*, 2002; *De Graaf et al.*, 2006]. These fires are mainly manmade to benefit agriculture. Smoke plays an important role as CCN, influencing cloud microphysics and precipitation processes. The presence of smoke plumes decreases cloud droplet sizes and increases the reflectivity of clouds [*Twomey*, 1959a; *Lohmann and Feichter*, 2005]. Smoke properties vary between fires depending on fuel type and moisture, combustion phase, flame temperature, wind conditions, and other variables [*Reid et al.*, 2005b; *Chambers et al.*, 2005; *Chen et al.*, 2006]. Smoke particles are usually internally mixed, typically with a core of black carbon and alkali earth compounds coated with organic compounds [*Martins et al.*, 1998; *Reid et al.*, 2005b]. Fresh smoke properties change rapidly and aged smoke properties, which are more of interest for global climate dynamics, are markedly different from fresh smoke properties but vary more slowly [*Abel et al.*, 2005; *Reid et al.*, 2005b]. Smoke particles are typically small but increase in size with age and aged particles are more spherical than fresh ones. Eighty percent of the mass and over 90 percent of scattering by smoke can be attributed to the fine mode [*Reid et al.*, 2005b].

[10] Small absorbing particles are very efficient in absorbing and scattering light, independent of their sizes. Therefore small quantities of light-absorbing particles can make a considerable contribution to the attenuation of light in the atmosphere [*Horvath*, 1993; *Reid et al.*, 2005a]. The aerosol component responsible for absorption in biomass burning is black carbon, or soot. Black carbon absorption depends weakly on wavelength over the near-UV to near-IR spectral region, where the soot imaginary refractive index is relatively constant [*Bergstrom et al.*, 2002; *Torres et al.*, 2005].

Table 1. Mie Calculation Parameters at 550 nm for a Log-Normal Size Distribution

	Size Parameters		Refractive Index	
Aerosol Model	r_{eff}, μm	v_{eff}	*Re*, (*m*)	*Im*, (*m*)
DDA fine mode	0.07	1.95	1.53	−0.0055[a]
DDA coarse mode	0.35	2.20		
BBA	0.08	1.45	1.55	−0.08
Water droplets	6.0	1.50	1.335[a]	0.0[a]

[a]Wavelength-dependent variable.

[11] In this paper, first the methods and data used for the analyses are described in section 2. A description of the desert dust and biomass burning aerosol scenes, the SCIAMACHY reflectance spectra of these scenes and the radiative transfer simulations are presented in section 3. The results and conclusions are discussed in section 4.

2. Methods and Data

2.1. Radiative Transfer Modeling

[12] Atmospheric reflectances were simulated using the Doubling-Adding KNMI (DAK) radiative transfer model [*Stammes*, 2001]. This model computes the monochromatic reflectance and transmittance in a plane-parallel atmosphere including polarization, using the polarized doubling-adding method [*De Haan et al.*, 1987]. This method calculates the vectorized internal radiation field of the atmosphere in an arbitrary number of layers, each of which can have Rayleigh scattering, gas absorption, and aerosol and cloud particle scattering and absorption. Only ozone absorption was accounted for, all other trace gases were ignored. For the atmospheric gas and temperature profiles 32 atmospheric layers were used, simulating the standard Midlatitude Summer atmosphere for scenes at latitudes greater than ±23°, and the standard Tropical atmosphere for scenes at latitudes less than ±23° [*Anderson et al.*, 1986]. The standard ground pressure was 1013 hPa and the standard ozone column 334 DU.

2.2. Mie Modeling

[13] The optical properties of aerosol and cloud particles in the model were calculated using Mie theory [*De Rooij and van der Stap*, 1984]. In each layer a monomodal or bimodal lognormal size distribution could be prescribed. In case of a bimodal size distribution, a weight function w defines the relative number of fine mode and coarse mode particles [*Bösche et al.*, 2006],

$$n_N(r) = w \cdot LN_f + (1 - w) \cdot LN_c, \quad (1)$$

where $n_N(r)$ is the number distribution and $LN_{f,c}$ is the lognormal size distributions for the fine and the coarse mode, constrained by the effective radius r_{eff} and the effective variance v_{eff} [cf. *Hansen and Travis*, 1974].

[14] The microphysical parameters used in this paper are given for 340, 550, and 1000 nm in Table 1. The effective radii and variances for the bimodal size distribution of the desert dust model were chosen similar to the small and large mode (monomodal size distribution) models of *Torres et al.* [1998], where the effective radii were fitted to the measurements, described in section 3.1. The real and imaginary parts of the refractive index were taken from *Hess et al.* [1998] for transported mineral aerosol, smoothed and interpolated to a 1 nm grid.

[15] A model for absorbing biomass burning aerosols was chosen similar to the carbonaceous models of *Torres et al.* [1998], where the effective radius was fitted to the measurements, described in section 3.2. The absolute value of the imaginary part of the refractive index for this aerosol model was 0.08, which represents extreme absorption and should be considered as an upper limit.

[16] Water droplets were simulated using a large effective radius and the real and imaginary parts of the refractive index were taken from *Palmer and Williams* [1974] (Table 1).

[17] In one case in section 3.2, an effective single scattering albedo was determined from the measurements, using a Henyey-Greenstein (HG) phase function [*Henyey and Greenstein*, 1941] instead of Mie calculations. In this way no knowledge of the refractive index is needed and the single scattering albedo can be directly determined from the measurements.

2.3. SCIAMACHY Reflectance Spectra

[18] SCIAMACHY is part of the payload of the European "Environment Satellite" Envisat, launched on 1 March 2002 by an Ariane-5 launch vehicle from the Guyana Space Centre into a polar orbit at about 800 km altitude, with an equator crossing time of 1000 LT for the descending node, orbiting the Earth every 100 min. SCIAMACHY is a spectrometer designed to measure sunlight, transmitted, reflected, and scattered by the Earth's atmosphere or surface, in eight channels from 240 to 2380 nm at a spectral

Table 2. Aerosol Optical Properties at 340, 550, and 1000 nm

		τ			ω_0			τ_{abs}		
Aerosol Model	Type	340	550	1000	340	550	1000	340	550	1000
DDA fine mode	Mie	1.34	1.06	0.54	0.87	0.96	0.97			
DDA coarse mode	Mie	0.64	0.68	0.73	0.64	0.85	0.93			
Desert dust	Bimodal Mie	1.98	1.74	1.27	0.79	0.92	0.95	0.42	0.14	0.06
BBA	Mie	0.64	0.30	0.083	0.72	0.66	0.46			
Water droplets	Mie	19.4	19.7	20.2	1.0	1.0	1.0			
1 Layered	Monomodal Mie	20.1	20.0	20.3	0.991	0.995	0.997	0.18	0.10	0.06
2 Internal mix	HG	20.0	20.0	20.0	0.968	0.992	0.999	0.64	0.16	0.02
3 External mix	Bimodal Mie	20.1	20.0	20.3	0.991	0.995	0.997	0.18	0.10	0.06

resolution of 0.2–1.5 nm [*Bovensmann et al.*, 1999]. The radiance is observed in two alternating modes, nadir and limb, yielding data blocks called states. The size of a nadir state is approximately 960 × 4870 km^2. In nadir mode, SCIAMACHY scans the Earth from east to west in 4 s by rotating one of its internal mirrors. The radiance measurements of the first six channels were used at an optical integration time (IT) of 1 s, to produce a continuous reflectance spectrum from 240–1750 nm. With this IT a state is divided into 13 swaths, which are divided into four pixels of approximately 240 × 30 km^2. The reflectance is defined as $R = \pi I/(\mu_0 E_0)$, where I is the radiance at TOA, E_0 is the solar irradiance at TOA perpendicular to the direction of the incident sunlight and μ_0 is the cosine of the solar zenith angle θ_0. The extraterrestrial solar irradiance is measured each day, once per 14 orbits.

[19] SCIAMACHY's reflectances are about 15–20% too low [*Acarreta and Stammes*, 2005; *Tilstra et al.*, 2005]; therefore calibration corrections were applied to the spectra using a smooth function through the correction factors in the UV supplied by *Tilstra et al.* [2005] and the correction factors in the visible and near-IR supplied by *Acarreta and Stammes* [2005]. Above 900 nm the correction function was kept constant. In addition, a correction for a calibration error caused by improper characterization of the instrument's polarization response function around 350 nm was applied [*Tilstra and Stammes*, 2005]. Reflectance jumps between neighboring channels were corrected by averaging the measurements where wavelengths of neighboring channels overlap.

2.4. SCIAMACHY AAI

[20] The AAI separates the radiance contrast at two wavelengths (λ_0,λ) in the UV caused by aerosol absorption from that caused by molecular Rayleigh scattering. It uses measured reflectances $R^{\text{meas}}_{\lambda_0,\lambda}$ and simulated reflectances for a Rayleigh atmosphere $R^{\text{Ray}}_{\lambda_0,\lambda}$ with an adjustable Lambertian surface albedo. The AAI is derived from the residue.

[21] The residue $r_{\lambda_0,\lambda}$ is usually defined as [*Herman et al.*, 1997; *Torres et al.*, 1998; *De Graaf et al.*, 2005]

$$r_{\lambda_0,\lambda} = -100 \cdot {}^{10}\log\left(\frac{R^{\text{meas}}_{\lambda}}{R^{\text{Ray}}_{\lambda}}\right), \tag{2}$$

with the assumption that the surface albedo A_s for which R^{Ray}_{λ} is calculated, satisfies

$$R^{\text{Ray}}_{\lambda_0}(A_s) = R^{\text{meas}}_{\lambda_0}, \tag{3}$$

where the surface albedo is assumed to be constant in the range [λ, λ_0]. The SCIAMACHY residue is calculated for λ = 340 nm and λ_0 = 380 nm, so this assumption is valid for most surfaces. Now $r_{\lambda_0,\lambda}$ can be expressed as

$$r_{\lambda_0,\lambda} = -100 \cdot \left\{ {}^{10}\log\left(\frac{R_{\lambda}}{R_{\lambda_0}}\right)^{\text{meas}} - \ {}^{10}\log\left(\frac{R_{\lambda}}{R_{\lambda_0}}\right)^{\text{Ray}} \right\}, \tag{4}$$

i.e., the difference between the slope of the measured reflectances and the slope of the Rayleigh reflectances at λ_0 and λ. Note that $R^{\text{Ray}}_{\lambda_0}$ and R^{Ray}_{λ} are dependent on the surface albedo, which changes for every scene. Therefore it is more convenient to eliminate the Rayleigh reflectances $R^{\text{Ray}}_{\lambda_0}$ and R^{Ray}_{λ} from equations (2) and (3) and express $r_{\lambda_0,\lambda}$ as a function of only the measured reflectances $R^{\text{meas}}_{\lambda_0}$ and $R^{\text{meas}}_{\lambda}$ and some atmospheric constants.

[22] In order to do so, the surface contribution to the reflectance at TOA is separated from that of the atmosphere, using the assumption that the atmosphere is bounded from below by a Lambertian surface, which reflects incident radiation uniformly and unpolarized in all directions [*Chandrasekhar*, 1960]:

$$R(\lambda, \mu, \mu_0, \phi - \phi_0, A_s) = R_0(\lambda, \mu, \mu_0, \phi - \phi_0) + \frac{A_s T(\lambda)}{1 - A_s s^*(\lambda)}. \tag{5}$$

The first term, R_0, is the path radiance, which is the atmospheric contribution to the reflectance, depending on the relative azimuth angle $\phi - \phi_0$. The second term is the azimuth-independent contribution of the surface with an albedo A_s. Here, $T = t(\mu)t(\mu_0)$, where t is the total atmospheric transmission, dependent on μ_0 and μ, which is the cosine of the viewing zenith angle θ and s^* is the spherical albedo of the atmosphere for illumination from below. Substituting equation (5) in equation (3), the surface albedo is expressed in terms of $R^{\text{meas}}_{\lambda_0}$,

$$A_s = \frac{R^{\text{meas}}_{\lambda_0} - (R_0)_{\lambda_0}}{T_{\lambda_0} + s^*_{\lambda_0}\left(R^{\text{meas}}_{\lambda_0} - (R_0)_{\lambda_0}\right)}. \tag{6}$$

When A_s is substituted in equation (5), the Rayleigh reflectance at wavelength λ is found,

$$R^{\text{Ray}}_{\lambda} = (R_0)_{\lambda} + \frac{T_{\lambda} \cdot \left(R^{\text{meas}}_{\lambda_0} - (R_0)_{\lambda_0}\right)}{T_{\lambda_0} + (s^*_{\lambda_0} - s^*_{\lambda})\left(R^{\text{meas}}_{\lambda_0} - (R_0)_{\lambda_0}\right)}. \tag{7}$$

Now R^{Ray}_{λ} can be eliminated from equation (2):

$$r_{\lambda_0,\lambda} = -100 \cdot {}^{10}\log\left(\frac{R^{\text{meas}}_{\lambda}}{(R_0)_{\lambda} + c_a}\right), \tag{8}$$

where

$$c_a = T_{\lambda} \cdot \left((s^*_{\lambda_0} - s^*_{\lambda}) + \frac{T_{\lambda_0}}{R^{\text{meas}}_{\lambda_0} - (R_0)_{\lambda_0}}\right)^{-1} \tag{9}$$

is the adjusted surface contribution. Equation (8) shows that the residue will be positive in cases where the measured scene reflectance is smaller than the sum of the path radiance and adjusted surface contribution. In case of a low surface reflectivity, this can be accomplished when the measured reflectance is decreased relative to the path radiance at λ, by absorption in the atmosphere. In the UV the path radiance is strongly wavelength dependent due to Rayleigh scattering, and even gray absorbers can reduce the reflectance stronger at λ compared to λ_0, where $\lambda < \lambda_0$ [*Torres et al.*, 1998; *De Graaf et al.*, 2005]. In case of a bright surface, however, the contribution of the path

radiance is small and the positive residue must be caused by a wavelength-dependent absorber.

[23] The AAI is defined as the positive part of the residue, which has been shown to be indicative for UV-absorbing aerosols [*Hsu et al.*, 1996; *Herman et al.*, 1997; *Torres et al.*, 1998; *De Graaf et al.*, 2005, 2006]. The SCIAMACHY AAI was used to find scenes with high aerosol loadings.

2.5. Surface Albedo Database

[24] The surface albedo used in the radiative transfer model was taken from the GOME spectral surface albedo database [*Koelemeijer et al.*, 2003]. With this database a surface reflectivity can be determined for the range 335–772 nm for an arbitrary area on the Earth's surface. At wavelengths larger than 772 nm the surface albedo was kept constant, which is a good approximation for ocean surfaces.

2.6. Cloud Detection

[25] For every SCIAMACHY pixel the effective cloud fraction and cloud pressure were determined using the Fast Retrieval Scheme for Clouds from the O_2 A-band (FRESCO) algorithm [*Koelemeijer et al.*, 2001; *Fournier et al.*, 2006], which makes use of the reflectance in and around the oxygen A-band at 760 nm. The algorithm uses simplified radiative transfer modeling to determine the amount of cloud and clear-sky reflected radiance, where the cloud is assumed to be a Lambertian reflector with albedo 0.8 and the clear sky is bounded from below by a Lambertian surface, the albedo of which is taken from the GOME spectral surface albedo database.

[26] Additionally, SCIAMACHY's Polarization Measurement Devices (PMDs) were used to create true color images. The PMDs have a higher spatial resolution (7.5×30 km^2) than the spectral channel measurements and were used to visually identify clouds. The PMD images are not shown here.

2.7. MODIS Aerosol Optical Thickness and RGB Images

[27] From Moderate Resolution Imaging Spectroradiometer (MODIS) aboard NASA's Terra satellite, the AOT at 550 nm was used to characterize the aerosol loading of the scenes. Terra/MODIS, launched at the end of 1999 into a polar orbit at about 700 km altitude, with an equator crossing time of 1030 LT for the descending node, is making near-global daily observations of the Earth. The AOT is available over both land and ocean, using different algorithms. Cloud and sunglint screening is performed before retrieving an AOT. The error of MODIS optical thickness retrievals are within ($\pm 0.03 \pm 0.05\ \tau$) over ocean and ($\pm 0.05 \pm 0.15\ \tau$) over land [*Remer et al.*, 2005].

[28] In addition to the MODIS AOT, true-color composites were created from MODIS bands 1, 4, and 3 (RGB), using reprojected level 1B granules mosaics with a desert style color enhancement. No quantitative information was extracted from these files, but they were used as a visual aid.

2.8. Back Trajectory Modeling

[29] Atmospheric back trajectories used in the analyses were calculated using the trajectory model TRAJKS [*Scheele et al.*, 1996; *Stohl et al.*, 2001]. TRAJKS is an off-line model, using three-dimensional European Centre for Medium-Range Weather Forecasts (ECMWF) L60 forecasting model data. L60 data have 60 vertical levels with a horizontal resolution of less than one degree. The time resolution of the input data is 6 hours. The output data are gridded to a $0.1^\circ \times 0.1^\circ \times 1$ hour grid.

3. Analyses

3.1. Desert Dust Scene

[30] A Saharan desert dust-blowing event on 25 July 2004 was selected to study the spectrum of a desert dust aerosol scene over a dark ocean surface, compared to that of a clear-sky ocean scene. In Figure 1a the horizontal distribution of SCIAMACHY AAI at 0915 UTC is overlaid on a MODIS RGB picture, acquired around 1110 UTC (right side of the plot) and 1250 UTC (left side of the plot). The black triangular area is the area outside the MODIS swath. The black rectangular contours depict the nadir states of SCIAMACHY within which data are available. Outside these states limb data or no data are available.

[31] In Figure 1b the MODIS AOT at 550 nm over land and ocean is overlaid over the same MODIS RGB picture as in Figure 1a. No MODIS AOT is retrieved over bright land surfaces, cloudy areas, and sunglint areas. In Figure 1 the left upper third of the picture is a sunglint area for MODIS' geometry.

[32] The blue and red rectangles are selected scenes for which the SCIAMACHY reflectance spectra were determined. The blue rectangle, the desert dust scene, was chosen where the SCIAMACHY AAI was greatest. The red rectangle, the clear-sky scene, was chosen so that the scene had almost the same geometry as the scene of the blue rectangle, but negative SCIAMACHY residue, and no clouds according to the PMD true color image. In contrast to the PMD image, the MODIS RGB picture shows remnants of the dust plume in the red rectangle and the MODIS AOT value was around 0.3–0.5. However, the MODIS data was acquired $3\frac{1}{2}$ hours after the SCIAMACHY data and the dust plume is spreading outward. Therefore the AOT in the red rectangle at the time of the SCIAMACHY overpass is assumed to be small. The average FRESCO effective cloud fraction for all pixels in the red rectangle was 3%.

[33] The reflectance spectra for the selected scenes are shown in Figure 2a. The bold red curve shows the clear-sky spectrum and the blue curve the desert dust spectrum. Also shown, in black, are simulated spectra for a pure Rayleigh atmosphere (dashed-dotted line), the simulated spectrum for an aerosol-laden atmosphere (solid line), and the surface albedo used in the simulations (dotted line). The aerosol-laden atmosphere was simulated with a bimodal size distribution of mineral aerosols in a layer between 3 and 4 km above the surface, which is a normal height for lofted mineral aerosols and sufficient to produce high AAIs. The geometries for both simulated scenes are the same as the geometries of the mean measured scenes.

[34] The measured clear-sky spectrum shows the opaque atmosphere for wavelengths below 300 nm due to ozone absorption, a peak in the reflectance and the Huggins band between 310 and 400 nm, and the strong decrease of the TOA reflectance with wavelength above 330 nm due to the λ^{-4} decrease of Rayleigh optical thickness. Above 500 nm, several oxygen and water vapor absorption bands can be

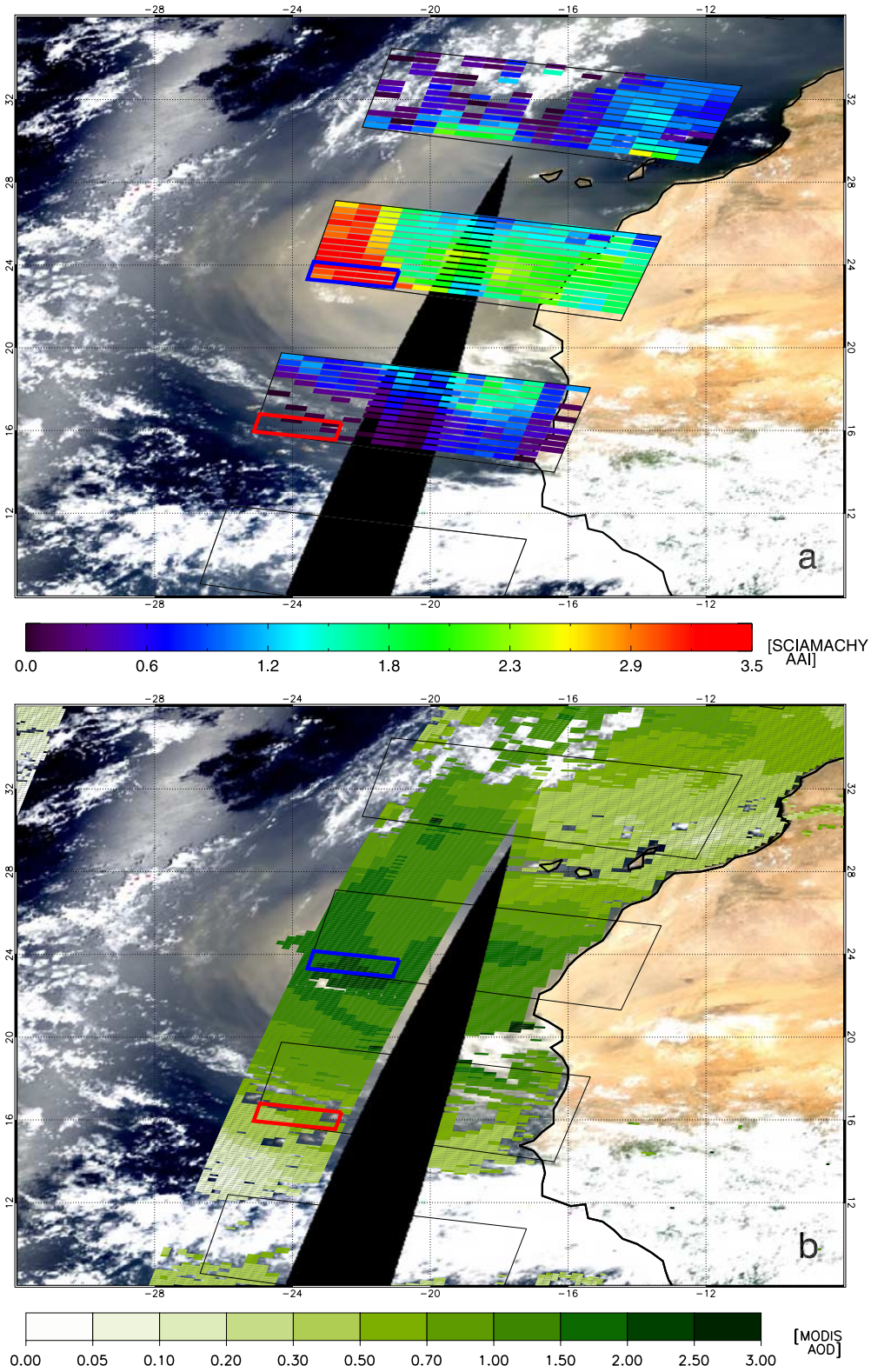

Figure 1. MODIS RGB image of dust storm on 25 July over west Sahara and eastern North Atlantic Ocean with (a) SCIAMACHY AAI and (b) with MODIS total AOT at 550 nm. The blue and red rectangles are the selected scenes, and the geometries [θ_0, θ, $\phi - \phi_0$] of the blue and red scenes are [24.7°, 28.7°, 189.9°] and [24.7°, 30.4°, 203.3°], respectively.

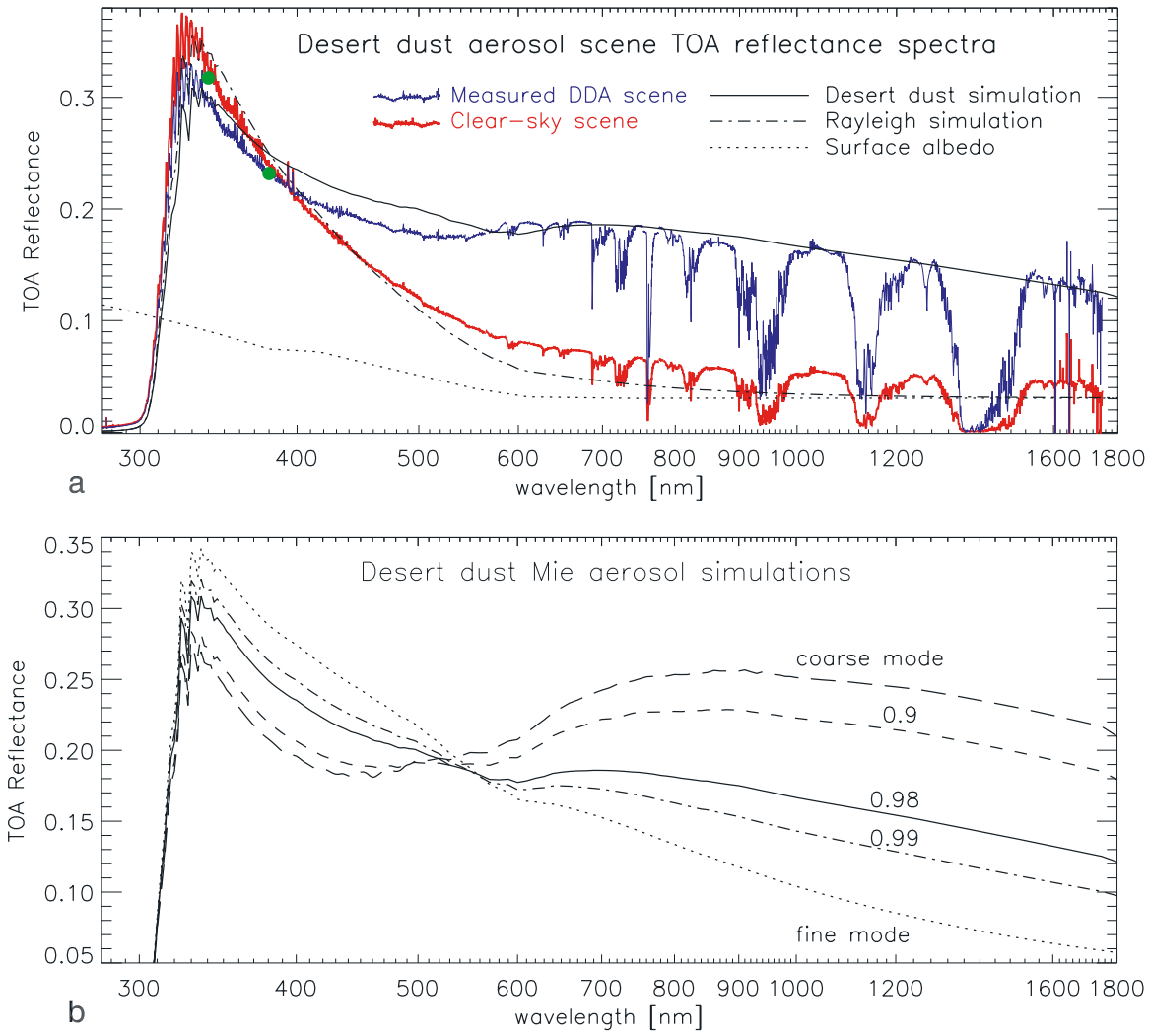

Figure 2. (a) Measured spectra of clear-sky (bold red) and desert dust (blue) scenes of Figure 1 and simulations using a bimodal mineral aerosol model (black solid line) and Rayleigh atmosphere model (black dashed-dotted line). The surface albedo used in the simulations is given by the dotted line. The green dots are the simulated Rayleigh atmosphere reflectances with adjusted surface albedo used in the residue calculations. (b) Multiple simulated bimodal mineral aerosol spectra for different weights of the coarse and fine mode. Given weight factors w refer to the number density.

observed. The reflectance drops to about 0.05 at 1750 nm, which is slightly higher than the modeled clear-sky reflectance, that is controlled by the surface albedo from the surface albedo database. This excess of reflectance might be due to aerosol scattering that is possibly still present in the clear-sky scene.

[35] The blue curve in Figure 2a shows the reflectance change due to the presence of desert dust aerosols in the atmosphere, when compared to the reflectance of the clear sky. Mineral aerosols are absorbing in the UV; below 400 nm the reflectance of the aerosol-laden scene is lower than that of the clear-sky scene. This change of the reflectance in the UV is used by the AAI. The AAI of the desert dust scene is 3.34, a high value indicative of the presence of UV-absorbing aerosols at a high altitude. The green dots in Figure 2a are the calculated Rayleigh reflectances R^{Ray} in the residue calculation, at 340 and 380 nm. At 380 nm, R^{Ray}_{380} is exactly equal to the measured scene reflectance R^{meas}_{380} (by definition), but at 340 nm R^{Ray}_{340} is larger than the measured scene reflectance, which is caused by the absorption of the large mineral aerosols in the UV and expressed by a positive residue. On the other hand, both points are more or less on the red clear-sky spectrum; therefore the residue of the clear sky is small.

[36] Above 400 nm the mineral aerosols are mainly scattering; the reflectance of the aerosol-laden scene is higher than that of the clear-sky scene.

[37] The real measured scene has a slightly lower reflectance than the modeled scene reflectance between 350 and 570 nm and higher around 600 nm. The amount of absorption in the UV and scattering at higher wavelengths, which peaks around 650 nm, increases with increasing particle size of the mineral aerosols. For small mineral aerosols the absorption in the UV is negligible and the scattering at larger wavelength is much smaller than for large mineral aerosols, as shown in Figure 2b, which

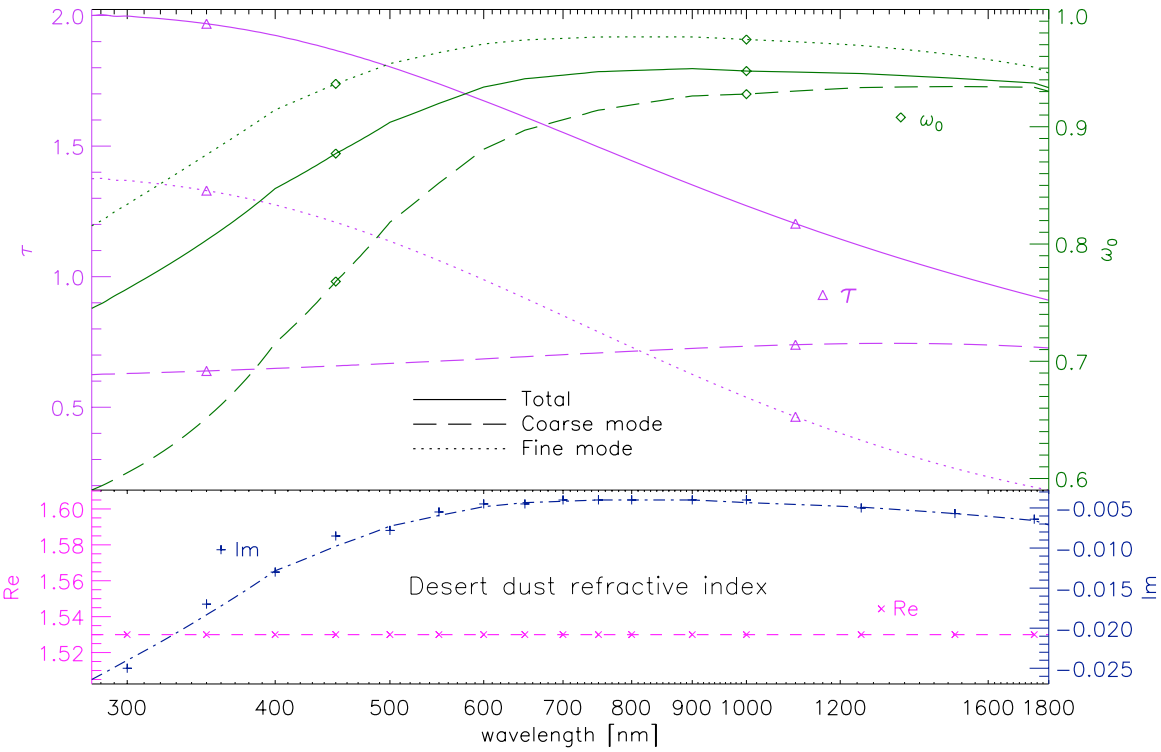

Figure 3. (top) Optical parameters for the desert dust model: Optical thickness (purple) and single scattering albedo (green) of the fine mode (dotted lines), coarse mode (dashed lines) and the total layer (solid line). (bottom) The real (magenta dashed line) and imaginary (blue dashed-dotted line) part of the refractive index used for the simulation of the bimodal mineral aerosol model. The plus signs refer to the data points given by *Hess et al.* [1998].

illustrates the contributions of the fine and coarse modes. The fine mode (dotted line) yields a continuously decreasing reflectance with increasing wavelength larger than 330 nm, not much different from the clear-sky spectrum. The coarse mode (long dashed line) on the other hand, is responsible for the absorption at UV wavelengths, while at wavelengths larger than 500 nm the scattering becomes dominant. For increasing weight factor w the absorption in the UV and the scattering at longer wavelengths decreases. A best fit to the measured spectrum was found using a weight w of 0.98, yielding a fine mode/coarse mode AOT fraction of 1.06/0.68 at 550 nm. This confirms the large fraction of the fine mode particles in a retrieved bimodal size distribution when using Mie theory to model mineral aerosols, found by AERONET data fits [*Dubovik et al.*, 2002a, 2002b].

[38] In Figure 3 the wavelength dependence of the optical thickness (purple, triangles) and the single scattering albedo (green, diamonds) are given for the fine mode (dotted lines), the coarse mode (dashed lines), and the total of the aerosol layer (solid lines). The wavelength dependence of the optical thickness of the aerosol layer is completely determined by the fine mode, which vanishes at near-IR wavelengths, while the absolute value of the AOT is determined by the weight of fine and the coarse mode. This was used to fit the AOT and the effective radius of the coarse mode at longer wavelengths. The best fit AOT was 1.74 at 550 nm, comparable to the MODIS AOT (see Figure 1b). The single scattering albedo of the coarse mode, on the other hand, is lower than that of the fine mode, showing again the larger contribution of the coarse mode particles to the absorption in the UV. For both the fine and the coarse modes the same refractive index was used, shown in the lower panel of Figure 3.

[39] Thus in the case of mineral aerosols the coarse mode is responsible for the UV absorption and the scattering in the visible and near-IR. The spectrum of the small mode shows a decreasing reflectance with wavelength, comparable to that of the clear-sky spectrum (Figure 2a). Therefore the AAI is sensitive to large mineral particles, but, using spherical particles, the shape of the spectrum cannot be fitted by a single coarse mode alone.

[40] With this fit of the mineral aerosol model to the measurements the absorption optical thickness can be estimated. The absorption optical thickness (τ_{abs}) is the part of the extinction optical thickness that is caused by absorption [*Torres et al.*, 2005]

$$\tau_{abs} = (1 - \omega_0)\tau. \quad (10)$$

This quantity was also derived for the desert dust scene (Table 2). It is strongly decreasing with wavelength, as both the single scattering albedo and the optical thickness of the aerosols are wavelength dependent. At 340 nm the absorption optical thickness is 0.42, which is 21% of the total AOT.

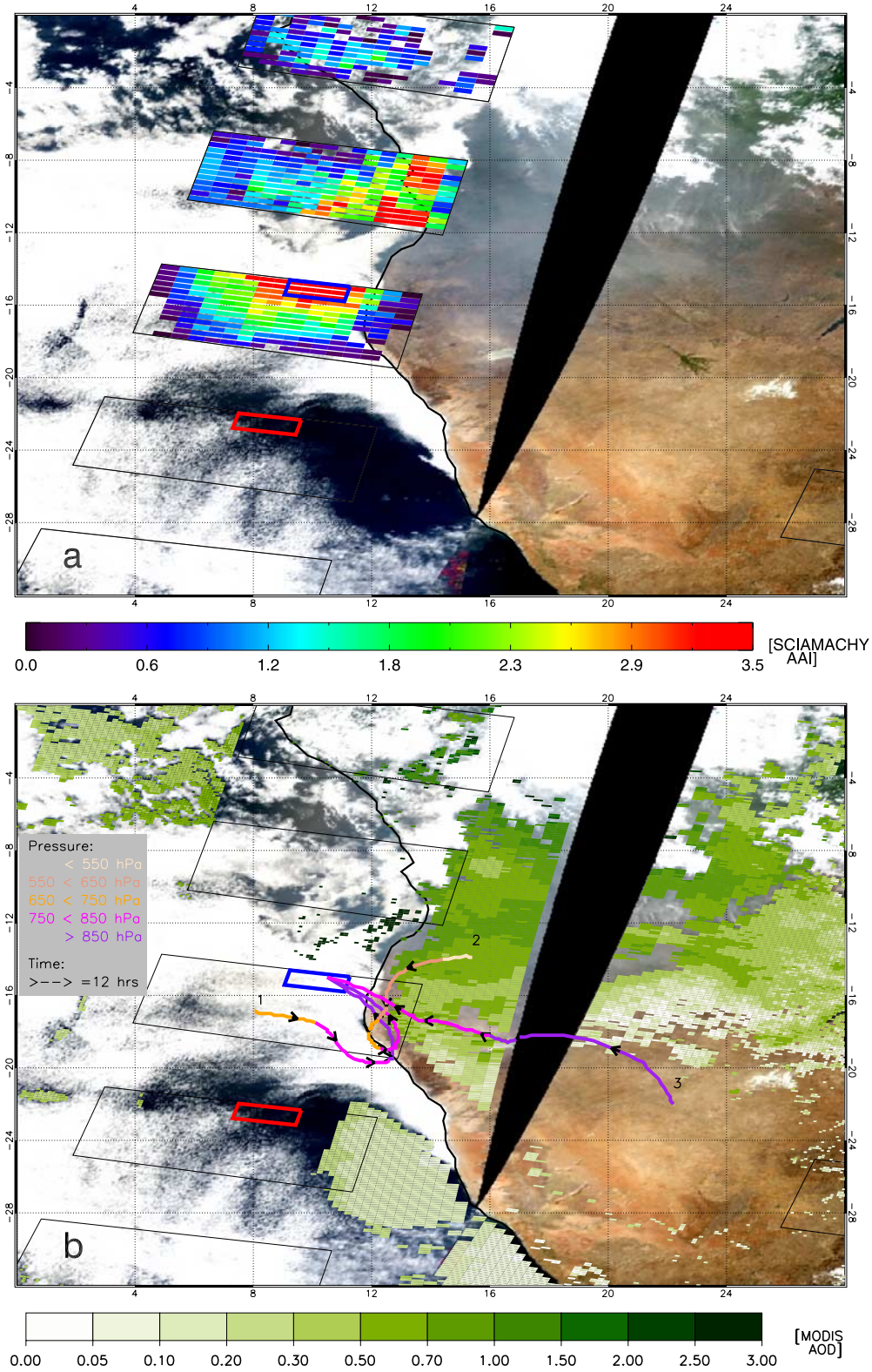

Figure 4. MODIS RGB image of biomass burning on 9 September 2004 over eastern South Atlantic Ocean with (a) SCIAMACHY AAI and (b) MODIS total AOT at 550 nm and TRAJKS back-trajectories. The blue and red rectangles are the selected scenes, the geometries $[\theta_0, \theta, \phi - \phi_0]$ of the blue and red scenes are [9.7°, 36.5°, 43.9°] and [9.7°, 41.6°, 50.3°], respectively.

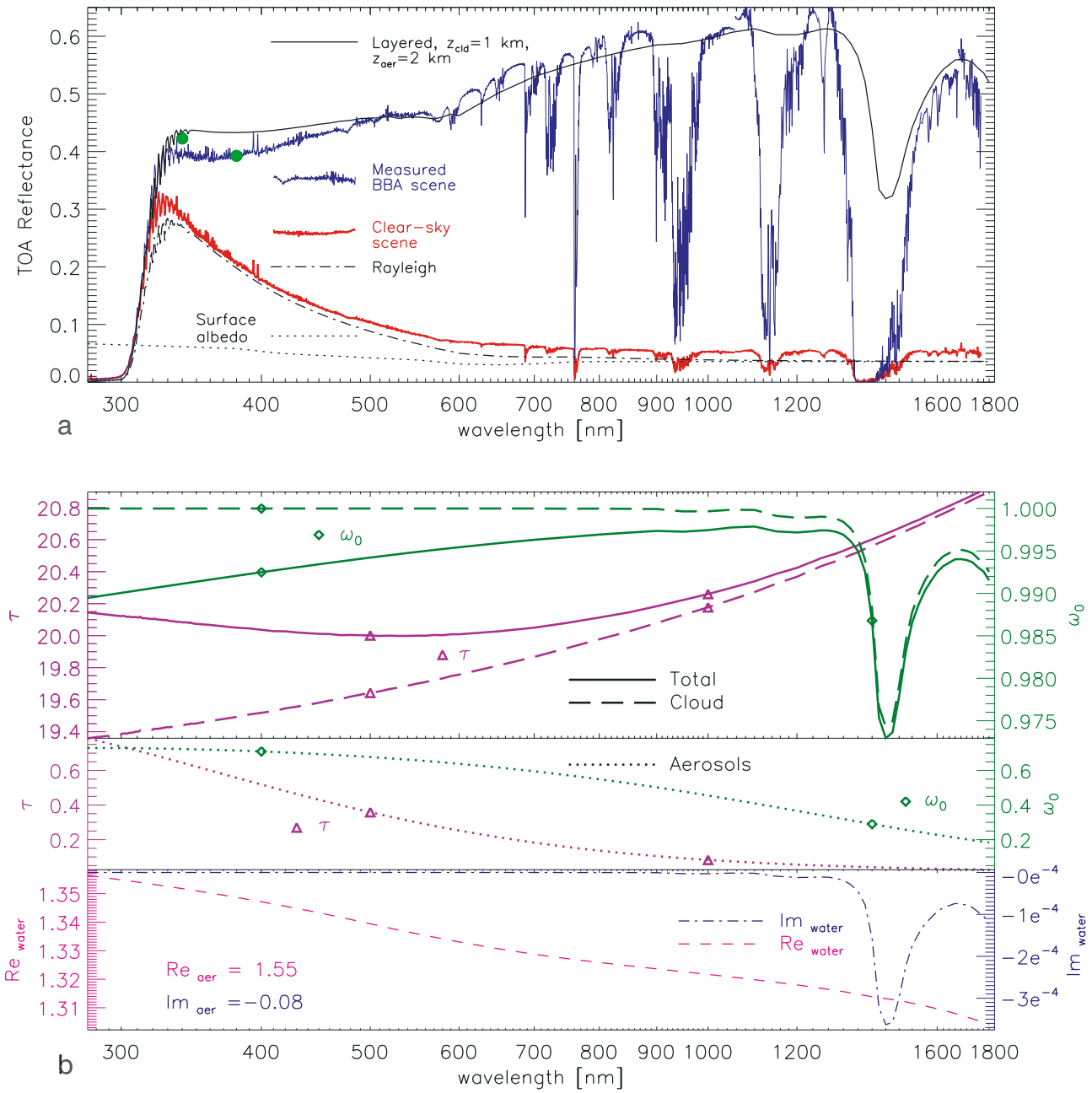

Figure 5. (a) Measured spectra of clear-sky (bold red) and biomass burning aerosol (blue) scenes of Figure 4 and simulation using a layered model (1) of BBA and cloud (black normal line). The simulation of the Rayleigh atmosphere is given by the dashed-dotted line and the surface albedo is given by the dotted line. The green dots are the simulated Rayleigh atmosphere reflectances with adjusted surface albedo used in the residue calculations. (b) Single scattering albedo (green) and optical thickness (purple) of the aerosols (dotted lines), cloud layer (dashed lines) and total for both layers (solid lines). The refractive index used for the Mie calculations is given in the lower panel.

3.2. Biomass Burning Scene

[41] An intense smoke scene on 9 September 2004, from a persistent biomass burning event over southwest Africa, was selected to study the spectrum of a biomass burning pollution scene with clouds over a dark ocean surface, compared to that of a clear-sky ocean scene. The smoke from this agricultural burning was extensive and could already be observed at the end of August 2004 and circulated over Angola and the adjacent South Atlantic Ocean for several weeks.

[42] In Figure 4 the SCIAMACHY AAI at 0912 UTC of 9 September 2004 is overlaid on a MODIS RGB picture, acquired around 0815 UTC (right side of the plot) and 0955 UTC (left side of the plot) of the same day. The black rectangular contours depict the nadir states of SCIAMACHY where data were available. The blue and red rectangles are the selected areas for which the reflectance

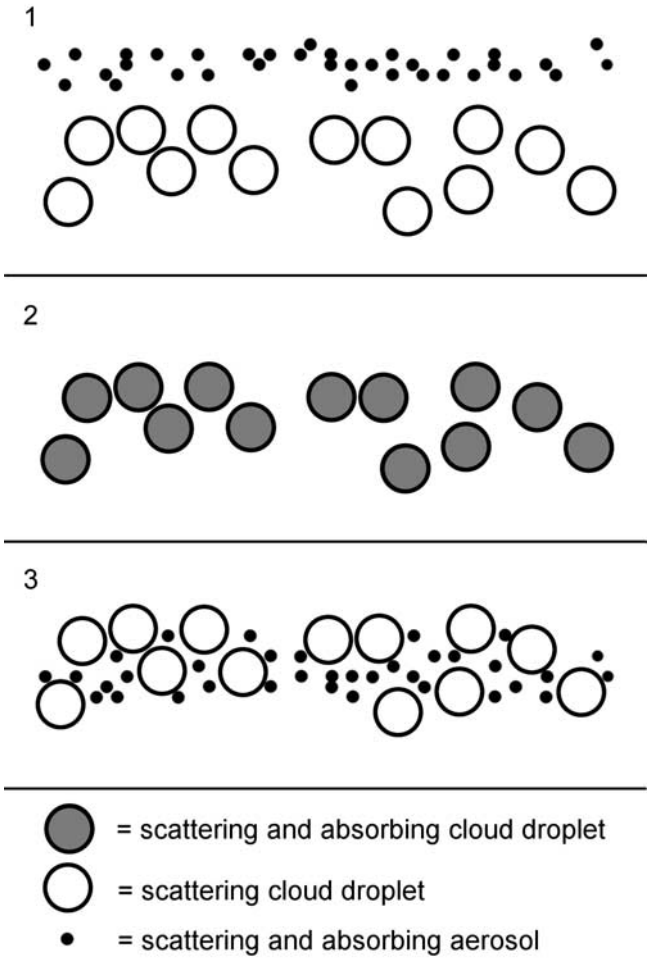

Figure 6. Three conceptual models of the distribution of cloud droplets and biomass burning aerosols in the polluted cloud scene. 1. Layered model. Cloud droplets and aerosols are in separate layers, with the cloud layer above the aerosol layer. 2. Internal mix. The aerosols are coated with water, resulting in cloud droplets with an absorbing core. 3. External mix. The cloud droplets and aerosols are mixed in the same layer, but not internally. The cloud droplets are large scattering aerosols and the aerosols are small absorbing aerosols.

spectra were determined. The blue rectangle was chosen where the SCIAMACHY AAI was greatest and the red rectangle was chosen so that the scene had almost the same geometry as the scene of the blue rectangle, but negative SCIAMACHY AAI, and no clouds according to the PMD true color image. The average FRESCO effective cloud fraction for all pixels in the red rectangle was 5%. The average FRESCO effective cloud fraction for all pixels in the blue rectangle was 72% and the average cloud top height 1.1 km.

[43] In Figure 4b the MODIS AOT at 550 nm over land and ocean is overlaid over the same MODIS RGB picture as in Figure 4a. Also shown are the back trajectories of air parcels arriving at the blue rectangle on 9 September 2004, 1200 UTC from 3 days before. Three back trajectories were computed, one of an air parcel which arrived at 1 km altitude (1), another parcel arriving at 1.5 km altitude (2), and one arriving at 2 km altitude (3). The pressure levels of the air parcels at certain times are given by the color scale, while the arrow heads denote the direction and the distance traveled in 12 hours.

[44] The trajectories show that air parcel 1 started at 3.5 km altitude over the ocean 3 days before 9 September 2004, made a turn over land to end in the blue rectangle, all the while losing altitude. Parcel 2 started over land in the heavily smoke covered area at 5 km altitude, first traveling southwest, making a 270° turn to the northwest on 9 September. The altitude of this parcel continuously decreased. Finally, parcel 3 started at 1.5 km altitude, traveled northwesterly all 3 days, gradually increasing in altitude.

[45] The smoke causing the high AAI in the blue rectangle was probably transported to this area at all altitudes, since the smoke plume over Angola was already observed over both land and ocean weeks before. Furthermore, the trajectories show that the marked land-ocean boundary in the cloud cover is probably caused by the flow of biomass burning aerosols from over land to the moist ocean. At all three altitudes the wind direction was southeasterly the last 12 hours before arriving at the blue rectangle, thereby crossing the land boundary. Since BBA are very effective CCN, they will immediately condense water when water vapor is available. Therefore it is likely that the blue rectangle scene contains a mixture of clouds and biomass burning aerosols.

[46] The MODIS RGB picture shows almost no remnants of smoke or clouds in the red rectangle and the MODIS AOT product (Figure 4b) also shows no AOT. Since the overpasses of MODIS and SCIAMACHY are within half an hour, the SCIAMACHY spectrum of the red rectangle scene can be assumed to be a clear-sky spectrum.

[47] The SCIAMACHY reflectance spectra of both scenes are plotted in Figure 5. The spectrum of the clear-sky scene (bold red line) is similar to the clear-sky scene of Figure 2, since essentially only the geometries are different. However, the spectrum of the polluted cloudy scene (blue line) shows a reflectance that is, outside gas absorption bands, continuously increasing with wavelength until about 1400 nm. Instead of the expected absorption in the UV, the reflectance is much larger than the clear-sky scene reflectance, and increasing with wavelength instead of decreasing, which was the case in Figure 2.

[48] The green dots in Figure 5a are again the calculated Rayleigh reflectances in the residue calculation, at 340 and 380 nm. The residue for this scene was comparable to that of the desert dust case, $r = 3.45$, but because of the bright scene, the adjusted surface contribution c_a that is used in the residue calculation (equation (8)) is now much higher (A_s = 0.33) than in the DDA case ($A_s = 0.046$). Since the surface albedo is not wavelength dependent, the reflectance difference of the green dots is much less than in the desert dust case, i.e., the slope of the spectrum is smaller.

[49] In order to understand the radiative transfer processes involved in a BBA polluted cloudy scene, three models for the mixture of aerosols and cloud droplets were constructed (Figure 6). The first model represents a scene with two separate layers, one with only BBA and one with cloud droplets. The second model represents a model of one layer, with an internal mixture of aerosols and cloud droplets, for

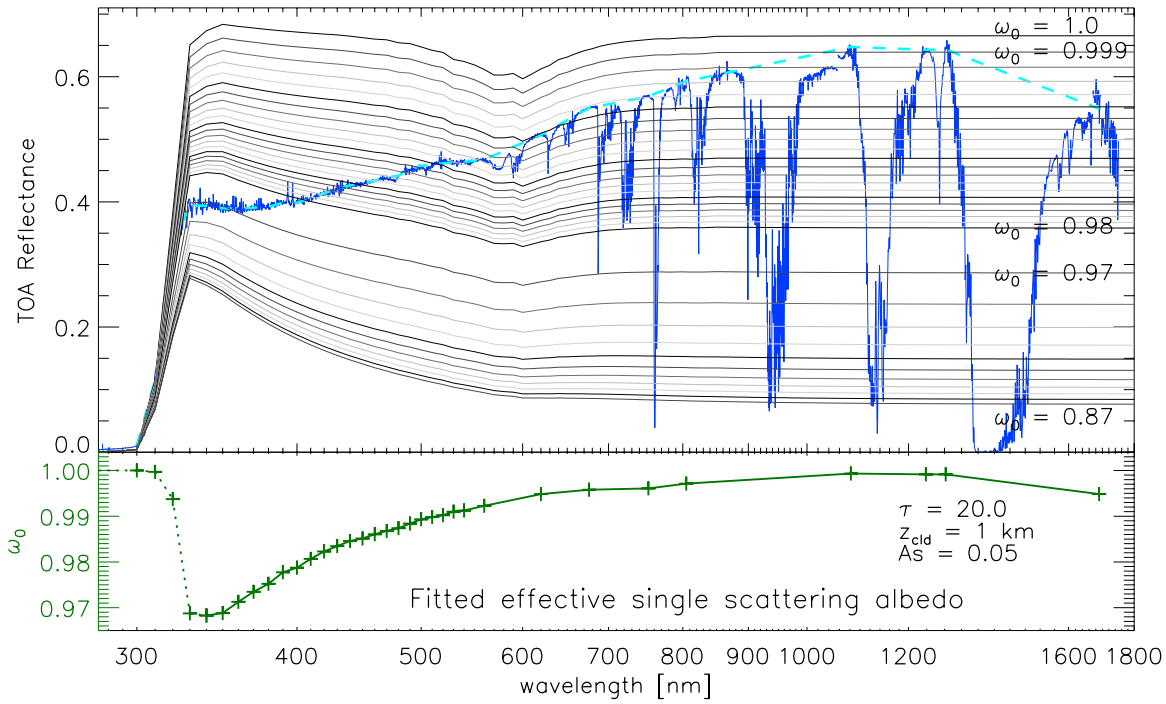

Figure 7. Cloud single scattering albedo fit for model 2. Top panel. Measured ocean biomass burning aerosol scene (blue), its envelope outside absorption bands (green) and simulations of polluted cloudy ocean scenes with increasingly lower single scattering albedo (gray scales). Lower panel. Retrieved single scattering albedo from the fit of the mean envelope of the measured spectrum (green line in top panel) to a simulated absorbing cloudy scene spectrum.

which an effective single scattering albedo is determined. Finally, the third model is a more sophisticated one-layer model, representing an external mix of water droplets and aerosols, with nonabsorbing water droplets and absorbing aerosols. In all models the thickness of the layers is 1 km and the total optical thickness of each model is always the same at 550 nm (see Table 2 for the layer parameters).

3.2.1. Model 1, Layered

[50] The spectrum of the two separate cloud and aerosol layers was fitted to the measurements using an aerosol optical thickness of 0.3 and a cloud optical thickness of 19.7. The optical properties of the cloud droplets and smoke aerosols were determined using Mie theory, with the size parameters listed in Table 1. The cloud was placed in the bottom one kilometer of the atmosphere and the aerosol layer was directly on top of the cloud layer. The spectrum of this scene is plotted in Figure 5a as the solid black line and simulates the measured scene reflectance outside absorption bands reasonably well. It is monotonically increasing with wavelength until about 1200 nm like the measured scene reflectance, although the slope is a little smaller. The drop in single scattering albedo around 1400 nm is due to absorption by the water droplets.

[51] In Figure 5b the wavelength dependence of the optical thickness (purple, triangles) and the single scattering albedo (green, diamonds) are given for the aerosols (dotted lines), the water droplets (dashed lines), and the total of both layers (solid lines). The values for 340, 550, and 1000 nm are also given in Table 2. The single scattering albedo of the aerosols is decreasing with wavelength, as was also retrieved from AERONET measurements for African savanna smoke aerosols [*Dubovik et al.*, 2002a]. The single scattering albedo of water droplets is one for the entire wavelength range, except around 1400 nm. However, the total single scattering albedo is increasing with wavelength due to the strong decrease of AOT with wavelength. In the UV the effect of absorption of the aerosols is much larger than at longer wavelengths because of the large value of AOT in the UV, even when the aerosol single scattering albedo decreases with wavelength.

[52] When an absorbing aerosol layer overlays a bright cloud, the reflection of radiation by the cloud is suppressed by the aerosol layer due to absorption in the aerosol layer and internal reflections between the scattering cloud and the absorbing aerosol layer. This suppression is strongest at shorter wavelengths, because of the increase of AOT with decreasing wavelength, which is measured by the AAI. Even when the total reflectance of cloud and aerosols is much higher in the UV than the clear-sky Rayleigh reflectance, the reflectance in the UV is still lower than that of a cloudy scene or a scene with a bright surface without aerosols. This is contrary to a cloudless aerosol scene with a high AAI, where the aerosols suppress the strongly wavelength-dependent Rayliegh scattering.

[53] Changing the height of the aerosol layer above the cloud did not change the simulated reflectance spectrum. This is also different from a cloudless aerosol scene, where the amount of suppressed Rayleigh scattering under the aerosol layer is partly determined by the height of the aerosol layer. In the current case all the cloud multiple scattering is below the aerosol layer. Of course, if the cloud was placed over the aerosol layer the opaque cloud reflected

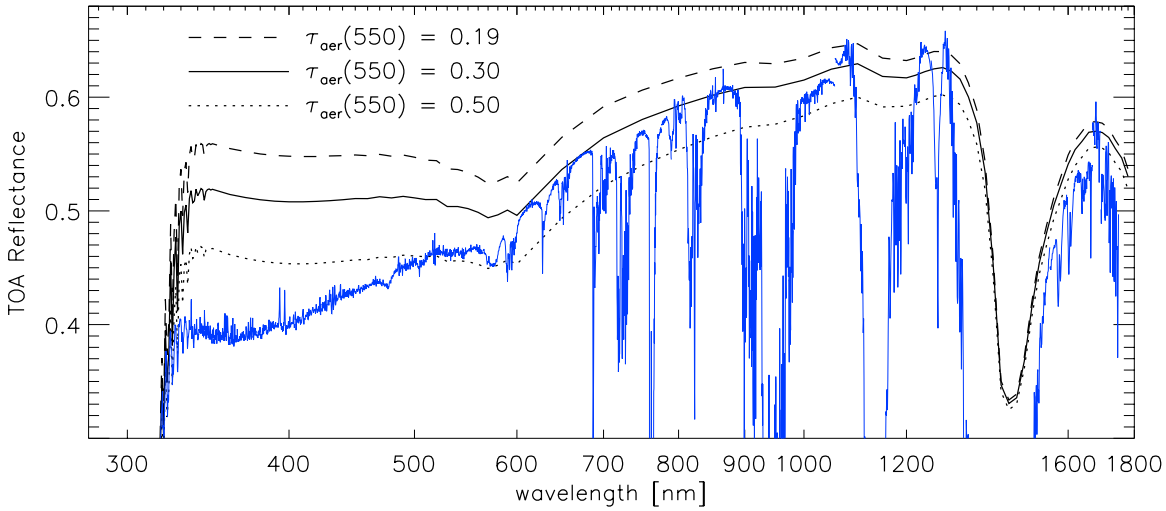

Figure 8. Multiple simulations of a smoke scene using model 3 (black lines), compared to the measured BBA scene (blue). The solid black line shows a fit to the measured reflectance spectrum, using a mixture of 99.5% aerosols in number density, corresponding to an aerosol optical thickness at 550 nm of 0.30, which is the same as the AOT of model 1. The reflectance spectra of layers with an AOT of 0.19 and 0.50 are shown for comparison by the dashed and the dotted line, respectively.

all incident radiation and the effect of aerosol absorption was nullified. The spectrum of a purely scattering cloud layer is plotted in Figure 7 with $\omega_0 = 1$.

3.2.2. Model 2, Internal Mix

[54] The spectrum could also be fitted to a one-layer model (model 2) with absorbing cloud droplets. A lookup table of simulated spectra of clouds with droplets having a range of gray (wavelength-independent) single scattering albedos was created, using a simple HG phase function for the cloud droplets, with $g = 0.85$. The cloud spectra were calculated using an optical thickness of the cloud of 20 at all wavelengths, a cloud top altitude of one kilometer and a surface albedo of 0.05. The spectra are plotted in greyscale in the top panel of Figure 7, together with the measured spectrum (blue).

[55] The spectral effective single scattering albedo of this model was fitted to an averaged envelope of the measured spectrum (cyan dashed line in top panel of Figure 7), representing the spectrum outside the absorption bands. The effective single scattering albedo (lower panel of Figure 7) is smallest around 340 nm at about 0.968 and increases with wavelength until about 1200 nm. The fitted single scattering albedo more or less follows the shape of the measured spectrum above 340 nm, which is not surprising since the individual simulated cloud spectra are almost horizontal lines, except in the O_3 Chappuis band around 600 nm. Below 340 nm the single scattering albedo can have any value, since the distinctions between the cloud spectra vanish due to the strong ozone absorption in the O_3 Hartley-Huggins band.

3.2.3. Model 3, External Mix

[56] The previous model (2) can be used to constrain the effective single scattering. However, to model the effect of individual cloud droplets and aerosol particles, a one-layer model with a bimodal size distribution (equation (1)), where the aerosols are the fine mode and the cloud droplets are the coarse mode, was created, using the size parameters given in Table 2. This represents an external mixture of cloud droplets and aerosols (model 3). The weight w controlled the relative number of aerosols and cloud particles, the optical thickness of the layer was 20 at 550 nm. The spectra for different AOTs are given in Figure 8.

[57] Using again an AOT of 0.30 at 550 nm (weight = 0.995), the reflectance spectrum can be modeled rather accurately outside absorption bands above about 600 nm, just like with model 1. Below 600 nm, however, the steep slope of reflectance with wavelength cannot be reproduced with model 3. The total single scattering albedos and optical thicknesses for this model are the same as those of model 1 (Table 2 and Figure 5b), but the suppression of cloud reflection in the UV for the mixed layer is less than when the aerosol layer is placed over the cloud layer. This is caused by the homogeneous distribution of aerosols through the layer, whereas the radiation is concentrated in the top of the optically thick layer. Consequently, only aerosols in the top part of the cloud will contribute to absorption of radiation and the effect of the wavelength dependence of the aerosol optical thickness is less than in model 1.

[58] The absorption optical thickness of the biomass burning scene is dependent on the model used to fit the spectrum (Table 2). The absorption optical thickness at 340 nm is 0.18 for both models 1 and 3, which is 0.9% of the total optical thickness of the cloud/aerosol layers and only slightly wavelength dependent. Using the simpler one-layer HG cloud model 2, the absorption optical thickness increases to 0.64 at 340 nm and decreases strongly with wavelength.

4. Discussion and Conclusions

[59] In this paper the presence of aerosols was demonstrated in both a cloud-free Saharan-dust ocean scene and a high-reflectance (cloud-contaminated) savanna-smoke ocean scene, using the AAI. The physical mechanism for

the AAI is different in cloud-free and cloud-contaminated scenes, due to the interaction between cloud droplets and aerosols. Understanding this interaction is important to further develop aerosol retrieval algorithms. Aerosols were not demonstrated before in cloud-contaminated scenes using space-borne reflectance measurements.

[60] SCIAMACHY TOA reflectance spectra of desert dust and biomass burning aerosol scenes were analyzed for the wavelength range 280–1750 nm. The measured desert dust reflectance spectrum was lower in the UV and higher at longer wavelengths than a clear-sky spectrum, due to absorption in the UV and scattering at longer wavelengths of large mineral particles. The desert dust spectrum was not critically determined by a particular set of parameters. Nevertheless, a bimodal size distribution of spheres was necessary to fit the spectrum. Although a bimodal distribution is also found from AERONET retrievals for transported desert dust, an artificially increased small mode is created by the assumption of spherical particles [*Dubovik et al.*, 2002b]. However, the application of a nonspherical model is beyond the scope of this paper.

[61] The measured reflectance spectrum of the biomass burning aerosol scene showed a high reflectance in the UV, increasing with wavelength. The suppression of cloud multiple scattering due to absorption by aerosols is more efficient in the UV because of the decreasing AOT with wavelength, even if the refractive index of smoke aerosols is wavelength independent [*Dubovik et al.*, 2002a; *Torres and Bhartia*, 1999], which yields an increasing single scattering albedo with wavelength. This decreases the reflectance in the UV compared to that of a normal cloud scene, which is measured by the AAI. The effect is strongest when an aerosol layer is placed above the cloud because in an optically thick cloud the radiation is concentrated in the top of the cloud. However, in a layer with an external mix of aerosol and cloud droplets the effect can also be observed.

[62] Cloud droplets that are internally mixed with smoke aerosols can also absorb the radiation in the cloud. The mass absorption efficiency of a black carbon particle coated with a water layer is generally greater than that of a pure black carbon particle because the nonabsorbing water shell increases the total cross-sectional area of the particle and focuses light toward the absorbing core [*Martins et al.*, 1998]. This is valid for particles with radii of around 0.1 μm with a shell in the same order of size, where the water droplets used in the current study had effective radii of 6 μm. However, additional absorption by water droplets or water-coated aerosols cannot be excluded.

[63] The suppression of cloud multiple scattering is stronger at shorter wavelengths for small (smoke) particles, due to the strong decrease of AOT with wavelength in the UV, which is detected by the AAI in the BBA polluted cloud case. Smoke was detected before over bright surfaces using the AAI over snow and ice scenes in Greenland [*Hsu et al.*, 1999a]. There, the high AAIs were attributed to suppression of wavelength-dependent Rayleigh scattered radiation between the surface and the aerosol layer. However, the present study shows that decrease of AOT with wavelength is a more likely mechanism for the high AAI value in case of a bright surface. This is in agreement with theoretical studies, showing a decreasing signal for gray aerosols in increasingly brighter scenes, and a steady signal for smoke aerosols with wavelength-dependent absorption coefficients [*De Graaf et al.*, 2005].

[64] The slope of the spectrum in the UV, and hence the AAI, did not change with the height of the aerosol layer above the cloud, as long as the aerosols are above the cloud, since multiple scattering by the cloud is dominant over Rayleigh scattering. This would imply that the AAI is capable of detecting small particles close to the surface over bright surfaces.

[65] The effect of desert dust in the scene, on the other hand, is the suppression of the strongly wavelength-dependent Rayleigh scattering by the coarse mode mineral particles, and to a lesser degree the wavelength-dependent (increasing) single scattering albedo of the mineral particles in the UV. The slope of the spectrum in the UV, and the value of AAI, is strongly dependent on the amount of Rayleigh scattering under the aerosol layer and thus the height of the aerosol layer [*Torres et al.*, 1998; *De Graaf et al.*, 2005]. However, if the optical properties of desert dust are strongly wavelength dependent in the UV, as suggested by *Sinyuk et al.* [2003], then desert dust can also be detected close to the ground [*Mahowald and Dufresne*, 2004].

[66] The spectrum presented for the desert dust case was a typical, often observed spectrum. Desert dust is usually found in warm, continental, cloudless air. Good estimates for the AOT can be found for these cases, using both ground-based and space-borne instruments, although the latter often need a dark surface, which can be a problem over deserts. In biomass burning cases the spectra are much more variable. The presented spectrum is found only for BBA scenes, but BBA scene spectra with reflectances decreasing with wavelength also occur frequently, and cannot easily be separated from desert dust scenes [*De Graaf et al.*, 2006]. Those BBA scenes, however, have a much lower AAI. An inspection of occurrences of different BBA scenes in 2004 suggests that cloudless BBA scenes over oceans never have an AAI larger than one. However, cloudless ocean BBA scenes are very hard to find, since clouds are formed almost immediately when BBA enter moist air (although the survey was performed with SCIAMACHY, which has a large footprint, 30×60 km^2). On the basis of this survey we conclude that ocean BBA scenes with a high AAI are invariably cloudy scenes, like the one presented in this paper. This suggests that clouds enhance the AAI signal and that these clouds are polluted clouds.

[67] The AAI method is therefore extremely suitable for the detection of aerosols in high reflectance scenes. AOT retrievals using radiance measurements usually neglect cloudy scenes. However, clouds and aerosols are closely linked, and our quantitative knowledge of aerosol-cloud interactions will greatly benefit from direct measurement of aerosol properties inside clouds. Unfortunately, the conversion of AAI measurements into AOT or other aerosol properties is hampered by the dependence of the AAI on many related aerosol and atmospheric parameters [*Herman et al.*, 1997; *Torres et al.*, 1998; *De Graaf et al.*, 2005].

[68] A quantitative measure of aerosol absorption using the AAI is the absorption optical thickness [*Torres et al.*, 2005]. In the present study the absorption optical thickness was derived using the various models. The absorption optical thickness of desert dust is strongly decreasing with wavelength, as both the single scattering albedo and the

optical thickness of the aerosols are wavelength dependent. The biomass burning case shows that the absorption optical thickness is dependent on the model used to fit the spectrum. The AAI and absorption optical thickness can be valuable quantities to estimate the amount of globally absorbed radiation in the atmosphere due to absorbing aerosols in cloudy scenes. However, in that case a good model is necessary to estimate the optical thickness and single scattering albedos of the aerosols and clouds.

[69] **Acknowledgments.** The MODIS team is acknowledged for the use of the MODIS data. M. Scheele is acknowledged for his help with the TRAJKS simulation and E. Bösche for his work on the bimodal size distribution calculations. The work was financed by the Netherlands Agency for Aerospace Programmes (NIVR).

References

Abel, S. J., H. J. Highwood, J. M. Haywood, and M. A. Stringer (2005), The direct radiative effect of biomass burning aerosols over southern Africa, *Atmos. Chem. Phys.*, *5*, 1999–2018.

Acarreta, J. R., and P. Stammes (2005), Calibration comparison between SCIAMACHY and MERIS onboard ENVISAT, *IEEE Geosci. Remote Sens. Lett.*, *2*(1), 31–35.

Ackerman, A. S., O. B. Toon, D. E. Stevens, A. J. Heymsfield, V. Ramanathan, and E. J. Welton (2000), Reduction of tropical cloudiness by soot, *Science*, *288*, 1042–1047, doi:10.1126/science.288.5468.1042.

Albrecht, B. (1989), Aerosols, cloud microphysics, and fractional cloudiness, *Science*, *245*, 1227–1230.

Anderson, G. P., S. A. Clough, F. X. Kneizys, J. H. Chetwynd, and E. P. Shettle (1986), AFGL atmospheric constituent profiles, *Tech. Rep. AFGL-TR-86-0110*, Air Force Geophys. Lab., Hanscom Air Force Base, Mass.

Bergstrom, R. W., P. B. Russell, and P. Hignett (2002), Wavelength dependence of the absorption of black carbon particles: Predictions and results from the TARFOX experiment and implications for the aerosol single scattering albedo, *J. Atmos. Sci.*, *59*, 567–577, doi:10.1175/1520-0469.

Bösche, E., P. Stammes, T. Ruhtz, R. Preusker, and J. Fischer (2006), Effect of aerosol microphysical properties on polarization of skylight: Sensitivity study and measurements, *Appl. Opt.*, *45*, 8790–8805.

Bovensmann, H., J. P. Burrows, M. Buchwitz, J. Frerick, S. Noël, V. V. Rozanov, K. V. Chance, and A. P. H. Goede (1999), SCIAMACHY: Mission objectives and measurement modes, *J. Atmos. Sci.*, *56*(2), 127–150, doi:10.1175/1520-0469.

Chambers, S. D., J. Beringer, J. T. Randerson, and F. S. Chapin III (2005), Fire effects on net radiation and energy partitioning: Contrasting responses of tundra and boreal forest ecosystems, *J. Geophys. Res.*, *110*, D09106, doi:10.1029/2004JD005299.

Chandrasekhar, S. (1960), *Radiative Transfer*, 393 pp., Dover, Mineola, N. Y.

Chen, L.-W. A., et al. (2006), Particle emissions from laboratory combustion of wildland fuels: In situ optical and mass measurements, *Geophys. Res. Lett.*, *33*, L04803, doi:10.1029/2005GL024838.

Chiapello, I., J. M. Prospero, J. R. Herman, and N. C. Hsu (1999), Detection of mineral dust over the North Atlantic Ocean and Africa with the Nimbus 7 TOMS, *J. Geophys. Res.*, *104*(D8), 9277–9292.

D'Almeida, G. A. (1986), A model for Saharan dust transport, *J. Clim. Appl. Meteorol.*, *24*, 903–916.

Darmenova, K., I. N. Sokolik, and A. Darmenov (2005), Characterization of east Asian dust outbreaks in the spring of 2001 using ground-based and satellite data, *J. Geophys. Res.*, *110*, D02204, doi:10.1029/2004JD004842.

De Graaf, M., P. Stammes, O. Torres, and R. B. A. Koelemeijer (2005), Absorbing Aerosol Index: Sensitivity Analysis, application to GOME and comparison with TOMS, *J. Geophys. Res.*, *110*, D01201, doi:10.1029/2004JD005178.

De Graaf, M., P. Stammes, and I. Aben (2006), Temporal and spectral variation of desert dust and biomass burning aerosol scenes from 1995–2000 using GOME, *Atmos. Chem. Phys. Disc.*, *6*, 1321–1353.

De Haan, J. F., P. B. Bosma, and J. W. Hovenier (1987), The adding method for multiple scattering calculations of polarized light, *Astron. Astrophys.*, *183*, 371–391.

De Rooij, W. A., and C. C. A. H. van der Stap (1984), Expansion of Mie scattering matrices in generalized spherical functions, *Astron. Astrophys.*, *131*, 237–248.

Diner, D. J., et al. (2001), MISR aerosol optical depth retrievals over Southern Africa during the SAFARI-2000 dry season campaign, *Geophys. Res. Lett.*, *28*(6), 3127–3130.

Dubovik, O., B. N. Holben, T. F. Eck, A. Smirnov, Y. J. Kaufman, M. D. King, D. Tanré, and I. Slutsker (2002a), Variability of absorption and optical properties of key aerosol types observed in worldwide locations, *J. Atmos. Sci.*, *59*(3), 590–608, doi:10.1175/1520-0469.

Dubovik, O., B. N. Holben, T. Lapyonok, A. Sinyuk, and M. I. Mishchenko (2002b), Non-spherical aerosol retrieval method employing light scattering by spheroids, *Geophys. Res. Lett.*, *29*(10), 1415, doi:10.1029/2001GL014506.

Duncan, B. N., I. Bey, M. Chin, L. J. Mickley, T. D. Fairlie, and R. V. Martin (2003), Indonesian wildfires of 1997: Impact on tropospheric chemistry, *J. Geophys. Res.*, *108*(D15), 4458, doi:10.1029/2002JD003195.

Eckardt, F. D., and N. Kuring (2005), SeaWiFS identifies dust sources in the Namib Desert, *Int. J. Remote Sens.*, *26*(19), 4159–4167, doi:10.1080/01431160500113112.

Fournier, N., P. Stammes, M. de Graaf, R. van der A, A. Piters, M. Grzegorski, and A. Kokhanovsky (2006), Improving cloud information over deserts from SCIAMACHY Oxygen A-band measurements, *Atmos. Chem. Phys.*, *6*, 163–172.

Gao, Y., Y. J. Kaufman, D. Tanré, D. Kolber, and P. G. Falkowski (2001), Seasonal distributions of aeolian iron fluxes to the global ocean, *Geophys. Res. Lett.*, *28*(1), 29–32.

Gleason, J. F., N. C. Hsu, and O. Torres (1998), Biomass burning smoke measured using backscattered ultraviolet radiation: SCAR-B and Brazilian smoke interannual variability, *J. Geophys. Res.*, *103*(D24), 31,969–31,978.

Hansen, J., Mki Sato, A. Lacis, and R. Ruedy (1997), The missing climate forcing, *Phil. Trans. Roy. Soc. London, Ser. B*, *352*, 231–240.

Hansen, J. E., and L. D. Travis (1974), Light scattering in plantary atmospheres, *Space Sci. Rev.*, *16*, 527–610.

Hauser, A., D. Oesch, N. Foppa, and S. Wunderle (2005), NOAA AVHRR derived aerosol optical depth over land, *J. Geophys. Res.*, *110*, D08204, doi:10.1029/2004JD005439.

Haywood, J., and O. Boucher (2000), Estimates of the direct and indirect radiative forcing due to tropospheric aerosols: A review, *Rev. Geophys.*, *38*(4), 513–543.

Henyey, L. G., and J. L. Greenstein (1941), Diffuse radiation in the galaxy, *Astrophys. J.*, *93*, 70–83.

Herman, J. R., P. K. Bhartia, O. Torres, C. Hsu, C. Seftor, and E. A. Celarier (1997), Global distributions of UV-absorbing aerosols from NIMBUS 7/TOMS data, *J. Geophys. Res.*, *102*(D14), 16,911–16,922.

Hess, M., P. Koepke, and I. Schult (1998), Optical Properties of Aerosols and Clouds: The software package OPAC, *Bull. Am. Meteorol. Soc.*, *79*, 831–844.

Horvath, H. (1993), Atmospheric Light Absorption – A review, *Atmos. Env.*, *27A*(3), 293–317.

Hsu, N. C., J. R. Herman, P. K. Bhartia, C. J. Seftor, O. Torres, A. M. Thompson, J. F. Gleason, T. F. Eck, and B. N. Holben (1996), Detection of biomass burning smoke from TOMS measurements, *Geophys. Res. Lett.*, *23*(7), 745–748.

Hsu, N. C., J. R. Herman, J. F. Gleason, O. Torres, and C. J. Seftor (1999a), Satellite detection of smoke aerosols over a snow/ice surface by TOMS, *Geophys. Res. Lett.*, *26*(8), 1165–1168.

Hsu, N. C., J. R. Herman, O. Torres, B. N. Holben, D. Tanré, T. F. Eck, A. Smirnov, B. Chatenet, and F. Lavenu (1999b), Comparison of the TOMS aerosol index with Sun-photometer aerosol optical thickness: Results and applications, *J. Geophys. Res.*, *104*(D6), 6269–6280.

Intergovernmental Panel on Climate Change (2001), *Climate Change 2001, The Scientific Basis*, edited by Houghton, J. T., et al., 295 pp., Cambridge Univ. Press, New York.

Kaufman, Y. J., D. Tanré, and O. Boucher (2002), A satellite view of aerosols in the climate system, *Nature*, *419*, 215–223, doi:10.1038/nature01091.

Kaufman, Y. J., I. Koren, L. A. Remer, D. Tanré, P. Ginoux, and S. Fan (2005), Dust transport and deposition observed from the Terra-Moderate Resolution Imaging Spectroradiometer (MODIS) spacecraft over the Atlantic Ocean, *J. Geophys. Res.*, *110*, D10S12, doi:10.1029/2003JD004436.

King, M. D. (2003), Cloud and aerosol properties, precipitable water, and profiles of temperature and water vapor from MODIS, *IEEE Trans. Geosci. Remote Sens.*, *41*(2), 442–458.

Koelemeijer, R. B. A., P. Stammes, J. W. Hovenier, and J. F. de Haan (2001), A fast method for retrieval of cloud parameters using oxygen a band measurements from the Global Ozone Monitoring Experiment, *J. Geophys. Res.*, *106*(D4), 3475–3490.

Koelemeijer, R. B. A., J. F. de Haan, and P. Stammes (2003), A database of spectral surface reflectivity in the range 335–772 nm derived from

5.5 years of GOME observations, *J. Geophys. Res.*, *108*(D2), 4070, doi:10.1029/2002JD002429.

Koren, I., Y. J. Kaufman, L. A. Remer, and J. V. Martins (2004), Measurement of the effect of biomass burning aerosol on inhibition of cloud formation over the Amazon, *Science*, *303*, 1342–1345, doi:10.1126/science.1089424.

Krotkov, N., P. Bhartia, J. Herman, J. Slusser, G. Labow, G. Scott, and G. Janson (2005), Aerosol ultraviolet absorption experiment (2002 to 2004), part 1: Ultraviolet multifilter rotating shadowband radiometer calibration and intercomparison with CIMEL sunphotometers, *Opt. Eng.*, *44*(4), doi:10.1117/1.1886818.

Kusmierczyk-Michulec, J., and G. de Leeuw (2005), Aerosol optical thickness retrieval over land and water using Global Ozone Monitoring Experiment (GOME) data, *J. Geophys. Res.*, *110*, D10S05, doi:10.1029/2004JD004780.

Lohmann, U., and J. Feichter (2005), Global indirect aerosol effects: A review, *Atmos. Chem. Phys.*, *5*.

Mahowald, N. M., and J.-L. Dufresne (2004), Sensitivity of TOMS aerosol aerosol index to boundary layer height: Implications for detection of mineral aerosol sources, *Geophys. Res. Lett.*, *31*, L03103, doi:10.1029/2003GL018865.

Martins, J. V., P. Artaxo, C. Liousse, J. S. Reid, P. V. Hobbs, and Y. J. Kaufman (1998), Effects of black carbon content, particle size, and mixing on light absorption by aerosols from biomass burning in Brazil, *J. Geophys. Res.*, *103*(D4), 32,041–32,050.

Okin, G. S. (2005), Dependence of wind erosion and dust emission on surface heterogeneity: Stochastic modeling, *J. Geophys. Res.*, *110*, D11208, doi:10.1029/2004JD005288.

Palmer, K., and D. Williams (1974), Optical properties of water in the near infrared, *J. Opt. Soc. Am.*, *64*, 1107–1110.

Patterson, E. M., D. A. Gillete, and B. H. Stockton (1977), Complex index of refraction between 300 and 700 nm for Saharan aerosol, *J. Geophys. Res.*, *82*, 3153–3160.

Prospero, J. M., and T. Carlson (1972), Saharan air outbreaks over the tropical North Atlantic, *Pure Appl. Geophys.*, *119*, 678–691.

Prospero, J. M., K. Barrett, T. Church, F. Dentener, R. A. Duce, H. Galloway, H. Levy II, J. Moody, and P. Quinn (1996), Atmospheric deposition of nutrients to the North Atlantic basin, *Biogeochem.*, *35*, 27–73.

Prospero, J. M., P. Ginoux, O. Torres, S. E. Nicholson, and T. E. Gill (2002), Environmental characterization of global sources of atmospheric soil dust identified with the Nimbus 7 Total Ozone Mapping Spectrometer (TOMS) absorbing aerosol product, *Rev. Geophys.*, *40*(1), 1002, doi:10.1029/2000RG000095.

Ramanathan, V., P. J. Crutzen, J. T. Kiehl, and D. Rosenfeld (2001), Aerosols, Climate, and the Hydrological Cycle, *Science*, *294*, 2119–2124, doi:10.1126/science.1064034.

Reid, J. S., T. F. Eck, S. A. Christopher, R. Koppmann, O. Dubovik, D. P. Eleuterio, B. N. Holben, E. A. Reid, and J. Zhang (2005a), A review of biomass burning emissions part III: Intensive optical properties of biomass burning particles, *Atmos. Chem. Phys.*, *5*.

Reid, J. S., R. Koppmann, T. F. Eck, and D. P. Eleuterio (2005b), A review of biomass burning emissions part II: Intensive physical properties of biomass burning particles, *Atmos. Chem. Phys.*, *5*.

Remer, L. A., et al. (2005), The MODIS aerosol algorithm, products and validation, *J. Atmos. Sci.*, *62*, 947–973, doi:10.1175/JAS3385.1.

Scheele, M. P., P. Siegmund, and P. van Velthoven (1996), Sensivity of trajectories to data resolution and its dependence on the starting point in or outside a tropopause fold, *Meteorol. Appl.*, *3*, 267–273.

Seftor, C. J., N. C. Hsu, J. R. Herman, P. K. Bhartia, O. Torres, W. I. Rose, D. J. Schneider, and N. Krotkov (1997), Detection of volcanic ash clouds from Nimbus 7/total ozone mapping spectrometer, *J. Geophys. Res.*, *102*(D14), 16,749–16,760.

Sinyuk, A., O. Torres, and O. Dubovik (2003), Combined use of satellite and surface observations to infer the imaginary part of the refractive index of Saharan dust, *Geophys. Res. Lett.*, *30*(D2), 1081, doi:10.1029/2002GL016189.

Sokolik, I., and O. B. Toon (1999), Incorporation of mineralogical composition into models of the radiative properties of mineral aerosol from UV to IR wavelengths, *J. Geophys. Res.*, *104*(D8), 9423–9444.

Spichtinger, N., M. Wenig, P. James, T. Wagner, U. Platt, and A. Stohl (2001), Satellite detection of a continental-scale plume of nitrogen oxides from boreal forest fires, *Geophys. Res. Lett.*, *28*(24), 4579–4582.

Stammes, P. (2001), Spectral radiance modelling in the UV-visible range, in *IRS 2000: Current Problems in Atmospheric Radiation*, edited by W. Smith and Y. Timofeyev, pp. 385–388, A. Deepak, Hampton, Va.

Stohl, A., L. Haimberger, M. P. Scheele, and H. Wernli (2001), An intercomparison of results from three trajectory models, *Meteorol. Appl.*, *8*, 127–135.

Tanré, D., M. Herman, and Y. J. Kaufman (1996), Information on aerosol size distribution contained in solar reflected spectral radiances, *J. Geophys. Res.*, *101*(D14), 19,043–19,060.

Tanré, D., F. M. Bréon, J.-L. Deuzé, M. Herman, P. Goloub, F. Nadal, and A. Marchand (2001), Global observation of anthropogenic aerosols from satellite, *Geophys. Res. Lett.*, *28*(24), 4555–4558.

Tilstra, L. G., and P. Stammes (2005), Alternative polarisation retrieval for SCIAMACHY in the ultraviolet, *Atmos. Chem. Phys.*, *5*, 2099–2107.

Tilstra, L. G., G. van Soest, and P. Stammes (2005), Method for in-flight satellite calibration in the ultraviolet using radiative transfer calculations, with application to Scanning Imaging Absorption Spectrometer for Atmospheric Chartography (SCIAMACHY), *J. Geophys. Res.*, *110*, D18311, doi:10.1029/2005JD005853.

Torres, O., and P. K. Bhartia (1999), Impact of tropospheric aerosol absorption on ozone retrieval from backscattered ultraviolet measurements, *J. Geophys. Res.*, *104*(D17), 21,569–21,578.

Torres, O., P. K. Bhartia, J. R. Herman, Z. Ahmad, and J. Gleason (1998), Derivation of aerosol properties from satellite measurements of backscattered ultraviolet radiation: Theoretical basis, *J. Geophys. Res.*, *103*(D14), 17,099–17,110.

Torres, O., P. K. Bhartia, J. R. Herman, A. Sinyuk, P. Ginoux, and B. Holben (2002), A long-term record of aerosol optical depth from TOMS observations and comparison to AERONET measurements, *J. Atmos. Sci.*, *59*(3), 398–413, doi:10.1175/1520-0469.

Torres, O., P. K. Bhartia, A. Sinyuk, and E. Welton (2005), Total Ozone Mapping Spectrometer measurements of aerosol absorption from space: Comparison to SAFARI 2000 ground-based observations, *J. Geophys. Res.*, *110*, D10S18, doi:10.1029/2004JD004611.

Twomey, S. A. (1959a), The nuclei of natural cloud formation. part II: The supersaturation in natural clouds and the variation of cloud droplet concentrations, *Geofis. Pure Appl.*, *43*, 243–249.

Twomey, S. A. (1959b), The nuclei of natural cloud formation. part I: The chemical diffusion method and its application to atmospheric nuclei, *Geofis. Pure Appl.*, *43*, 227–242.

Veefkind, J. P., G. de Leeuw, P. Stammes, and R. B. A. Koelemeijer (2000), Regional distribution of aerosol over land, derived from ATSR-2 and GOME, *Remote Sens. Environ.*, *74*, 377–386.

Veihelmann, B., H. Volten, and W. J. van der Zande (2004), Light reflected by an atmosphere containing irregular mineral dust aerosol, *Geophys. Res. Lett.*, *31*, L04113, doi:10.1029/2003GL018229.

Waquet, F., J.-F. Léon, P. Goloub, J. Pelon, D. Tanré, and J.-L. Deuzé (2005), Maritime and dust aerosol retrieval from polarized and multispectral active and passive remote sensors, *J. Geophys. Res.*, *110*, D10S10, doi:10.1029/2004JD004839.

M. de Graaf and P. Stammes, Royal Netherlands Meteorological Institute, P.O. Box 201, 3730 AE, De Bilt, Netherlands. (graafdem@knmi.nl)

E. A. A. Aben, Netherlands Institute for Space Research (SRON), Sorbonnelaan 2, 3584 CA Utrecht, Netherlands.